A Spatially Resolved Study of Hard X-Ray Emission in Kepler's Supernova Remnant: Indications of Different Regimes of Particle Acceleration

Vincenzo Sapienza[1,2] , Marco Miceli[1,2] , Aya Bamba[3,4] , Satoru Katsuda[5] , Tsutomu Nagayoshi[5], Yukikatsu Terada[5] , Fabrizio Bocchino[2] , Salvatore Orlando[2] , and Giovanni Peres[1,2]

[1] Dipartimento di Fisica e Chimica E. Segré, Universitá degli Studi di Palermo, Piazza del Parlamento 1, 90134, Palermo, Italy; vincenzo.sapienza@inaf.it
[2] INAF-Osservatorio Astronomico di Palermo, Piazza del Parlamento 1, 90134, Palermo, Italy
[3] Department of Physics, The University of Tokyo, 7-3-1 Hongo, Bunkyo, Tokyo 113-0033, Japan
[4] Research Center for the Early Universe, School of Science, The University of Tokyo, 7-3-1 Hongo, Bunkyo-ku, Tokyo 113-0033, Japan
[5] Graduate School of Science and Engineering, Saitama University, 255 Shimo-Okubo, Sakura, Saitama 338-8570, Japan

Abstract

Synchrotron X-ray emission in young supernova remnants (SNRs) is a powerful diagnostic tool to study the population of high-energy electrons accelerated at the shock front and the acceleration process. We performed a spatially resolved spectral analysis of NuSTAR and XMM-Newton observations of the young Kepler's SNR, aiming to study in detail its nonthermal emission in hard X-rays. We selected a set of regions all around the rim of the shell and extracted the corresponding spectra. The spectra were analyzed by adopting a model of synchrotron radiation in the loss-limited regime, to constrain the dependence of the cutoff energy of the synchrotron radiation on the shock velocity. We identify two different regimes of particle acceleration, characterized by different Bohm factors. In the north, where the shock interacts with a dense circumstellar medium (CSM), we found a more efficient acceleration than in the south, where the shock velocity is higher and there are no signs of shock interaction with the dense CSM. Our results suggest an enhanced efficiency of the acceleration process in regions where the shock–CSM interaction generates an amplified and turbulent magnetic field. By combining hard X-ray spectra with radio and γ-ray observations of Kepler's SNR, we modeled the spectral energy distribution. In the light of our results we propose that the observed γ-ray emission is mainly hadronic and originates in the northern part of the shell.

Unified Astronomy Thesaurus concepts: Cosmic ray sources (328); Supernova remnants (1667)

1. Introduction

Blast-wave shocks in supernova remnants (SNRs) are sites of particle acceleration and are believed to be the primary source of galactic cosmic rays (CRs). For shocks in supernova remnants (SNRs), the main acceleration mechanism is the diffusive shock acceleration (DSA; Bell 1978; Axford et al. 1977; Blandford & Ostriker 1978). The first evidence for high-energy ($E > 10^{12}$ eV) electrons accelerated in SNR shocks came with the detection of nonthermal X-ray emission of SN 1006 (Koyama et al. 1995). As a matter of fact the study of X-ray synchrotron emission of SNRs can provide helpful insights about the acceleration process, such as the shape of the electron energy distribution and the mechanisms that limit the maximum energy that electrons can reach. Different mechanisms can be invoked to limit the maximum electron energy in the acceleration process (Reynolds 2008); for example, it can be limited by radiative losses (*loss-limited* scenario) or by the finite acceleration time available (*age-limited* scenario).

Kepler's SNR owes its name to Johannes Kepler, who extensively studied its parent supernova (SN 1604). This remnant has a roughly spherical shape with an angular radius of approximately $1.8'$ with two characteristic protrusions (also called "ears"), one located in the southeast of the shell and the other located in the northwest. The SNR is very likely the result of a type Ia SN (Kinugasa & Tsunemi 1999). Reynolds et al. (2007)

found that Kepler's SNR is interacting with the nitrogen-rich circumstellar medium (CSM) in the north and suggest a single-degenerate scenario for the explosion (with the companion possibly being a runaway AGB star; see Bandiera 1987; Velázquez et al. 2006; Chiotellis et al. 2012; Kasuga et al. 2021), albeit there is no evidence for a survived companion star (Kerzendorf & Sim 2014; Ruiz-Lapuente et al. 2018).

Reynoso & Goss (1999) derived a distance of 4.8 ± 1.4 kpc, based on H I absorption from radio observations, while Aharonian et al. (2008) suggested a lower limit of 6.4 kpc motivated by the lack of a detectable γ-ray flux. However, recent estimates based on proper-motion measurements derived a distance $d = 5.1^{+0.8}_{-0.7}$ kpc (Sankrit et al. 2016). We then adopt $d = 5$ kpc throughout this paper.

Prominent particle acceleration in Kepler's SNR is testified by its energetic nonthermal emission. The detection of GeV γ-ray emission from Kepler's SNR was recently presented by Xiang & Jiang (2021) and interpreted as a signature of hadronic emission. Similar conclusions were reported by Acero et al. (2022) who propose the hadronic emission to originate in the northern part of the shell, while synchrotron and Inverse Compton emission are interpreted as originating in the southern regions. Prokhorov et al. (2022) reported the detection of very-high-energy (VHE) γ-ray emission from Kepler's SNR with the High Energy Stereoscopic System (HESS) telescope.

The presence of nonthermal X-ray emission in Kepler's SNR was first discovered in its southeastern region by Cassam-Chenaï et al. (2004), using an XMM-Newton observation. Reynolds et al. (2007) conducted spectral analysis in several regions of Kepler's SNR confirming that some of them are

dominated by synchrotron radiation. Recently, Nagayoshi et al. (2021) reported the first robust detection of hard X-ray emission, in the 15–30 keV band, by analyzing a Suzaku Hard X-ray Detector (HXD) observation. Several spatially resolved studies found that the roll-off frequency of the synchrotron radiation in Kepler's SNR lies in the range $\nu_r \sim 1$–8×10^{17} Hz (Cassam-Chenaï et al. 2004; Bamba et al. 2005; Nagayoshi et al. 2021). One can estimate if the cutoff energy ($E_{\max}$) of the synchrotron emitting electrons is loss-limited or time-limited by comparing the timescale for synchrotron losses (τ_{sync}) with the age of the remnant ($t_{age} = 418$ yr). The timescale for synchrotron cooling is,

$$\tau_{\mathrm{sync}} \approx 1700 \left(\frac{h\nu_r}{1 \text{ eV}}\right)^{-\frac{1}{2}} \left(\frac{B}{100 \ \mu\text{G}}\right)^{-\frac{3}{2}} \text{ yr.} \tag{1}$$

On the basis of the one-zone model of the broadband spectral energy distribution (SED), Nagayoshi et al. (2021) adopted a magnetic field of $\sim 40 \ \mu$G and a roll-off frequency $\nu_r = 1 \times 10^{17}$ Hz, corresponding to $\tau_{\mathrm{sync}} \sim 330$ yr. Nonlinear DSA predicts an amplification of the magnetic field strength as a result of the flux of kinetic energy of the cosmic rays streaming ahead of the shock (Bell 2004). Estimates of the magnetic field strength in Kepler's SNR, based on the thickness of the X-ray synchrotron filaments, provide values in the range of 170–250 μG (Völk et al. 2005; Parizot et al. 2006; Rettig & Pohl 2012; Reynolds et al. 2021). Assuming a value of magnetic field of 170 μG and the roll of frequency measured by Nagayoshi et al. (2021) we obtain $\tau_{\mathrm{sync}} \sim 30$ yr. In any case, the synchrotron cooling time is always lower than the age of Kepler's SNR, and we can therefore consider the loss-limited scenario as the most appropriate for this source.

Tsuji et al. (2021) measured the cutoff photon energy in different regions of several SNRs, Kepler's SNR among them, by describing the nonthermal X-ray emission with the loss-limited model proposed by Zirakashvili & Aharonian (2007). In this model, the cutoff photon energy (ϵ_0) is related to the shock speed, v_{sh}, through $\epsilon_0 \propto v_{\mathrm{sh}}^2 \eta^{-1}$, where η, or the Bohm diffusing factor, is the ratio between the diffusion coefficient and $c\lambda/3$ (where λ is the Larmor radius; the minimum value $\eta = 1$ corresponds to the Bohm limit) and is strongly related to the turbulence of the magnetic field, which scatters the charged particles. Tsuji et al. (2021) studied the dependence of ϵ_0 on v_{sh}, with a spatially resolved spectral analysis in order to estimate η in different remnants. However, the spatially resolved analysis of Kepler's SNR lacks the hard part of the spectrum, and the ϵ_0–v_{sh} plot shows a clear trend only for synchrotron-dominated regions, while no correlation can be found for other regions. Lopez et al. (2015) performed a similar analysis using a deep NuSTAR observation of Tycho's SNR. They found that in Tycho's SNR the highest-energy electrons are accelerated at the fastest shocks, with a steep dependence of the roll-off frequency on the shock speed.

In this paper, we present the first analysis of archive NuSTAR observations of Kepler's SNR. We exploit the high sensitivity of the NuSTAR telescope to study the morphological and spectral properties of the hard X-ray emission. We also perform a spatially resolved measurement of the cutoff energy of the synchrotron radiation, combining the NuSTAR data with an XMM-Newton observation, which allows us to get physical insights on the origin of nonthermal emission. We

describe the data reduction in Section 2. Section 3 is dedicated to the results of image and spectral analysis. The discussion and conclusions are presented in Sections 4 and Section 5, respectively.

2. Data Reduction

2.1. NuSTAR Observation

The NuSTAR observation of Kepler's SNR was performed from 2014 October 7 for an exposure time of 246 ks (Obs. ID: 40001020002, PI: F. Harrison), with pointing coordinates $\alpha_{J2000} = 17^{\mathrm{h}}30^{\mathrm{m}}36\overset{\mathrm{s}}{.}4$ and $\delta_{J2000} = -21°30'13''$. We processed the data using `nupipeline` of the NuSTAR Data Analysis Software (NuSTARDAS version 2.0.0 with CALDB version 20210202) included in HEAsoft version 6.28.

The maps shown in this paper were obtained by summing the photon counts detected in each pixel by the two Cadmium–Zinc–Telluride (CZT) detectors Focal Plane Modules A and B (FPMA and FPMB) in a given energy band. We performed a spatially resolved spectral analysis for both FPMA and FPMB by extracting the spectra from different regions of the remnant using the `nuproducts` pipeline for an extended source. Spectra were rebinned to have at least 25 counts per bin. For each region, FPMA and FPMB spectra were fitted simultaneously. We used the `nuproducts` pipeline to produce the redistribution matrix file (RMF) and the ancillary response file (ARF), and to extract the background spectrum. For the background, we selected an extraction region for each spectrum, outside of the shell and in the same chip as the source extraction region.

2.2. XMM-Newton Observation

We complemented NuSTAR data analysis with the analysis of an XMM-Newton European Photon Imaging Camera (EPIC) observation of Kepler's SNR, performed from 2020 March 19 for an exposure time of 140 ks (Obs. ID: 0842550101, PI: T. Sato). The observation has pointing coordinates $\alpha_{J2000} = 17^{\mathrm{h}}30^{\mathrm{m}}36\overset{\mathrm{s}}{.}9$, $\delta_{J2000} = -21°30'01''\!.1$, and was performed with the thick filter, in full-frame mode for the EPIC MOS cameras, and in large-window mode for the EPIC pn camera.

We processed the observation data files (ODF) using the `emproc` and the `epproc` tasks of the Science Analysis System (SAS) software, version 18.0.0, respectively, for the MOS and the pn cameras. The obtained event files were filtered for soft-proton contamination using the `espfilt` task, thus obtaining a screened exposure time of 108.2 ks for MOS 1, 110.1 for MOS 2 and 94.7 ks for the pn camera. Images were background subtracted by adopting the double-subtraction procedure described in Miceli et al. (2006), retaining only events with `FLAG=0` and `PATTERN ⩽12`. With this method we removed instrumental particles and diffuse X-ray background from the images by using the Filter Wheel Closed (FWC)[6] and the Blank Sky (BS)[7] files available at the XMM ESAC web pages. Count-rate images were obtained by mosaicking MOS 1 and MOS 2 maps and are vignetting corrected and adaptively smoothed (with the `asmooth` task) to a signal-to-noise ratio of 10.

---

[6] https://www.cosmos.esa.int/web/xmm-newton/filter-closed
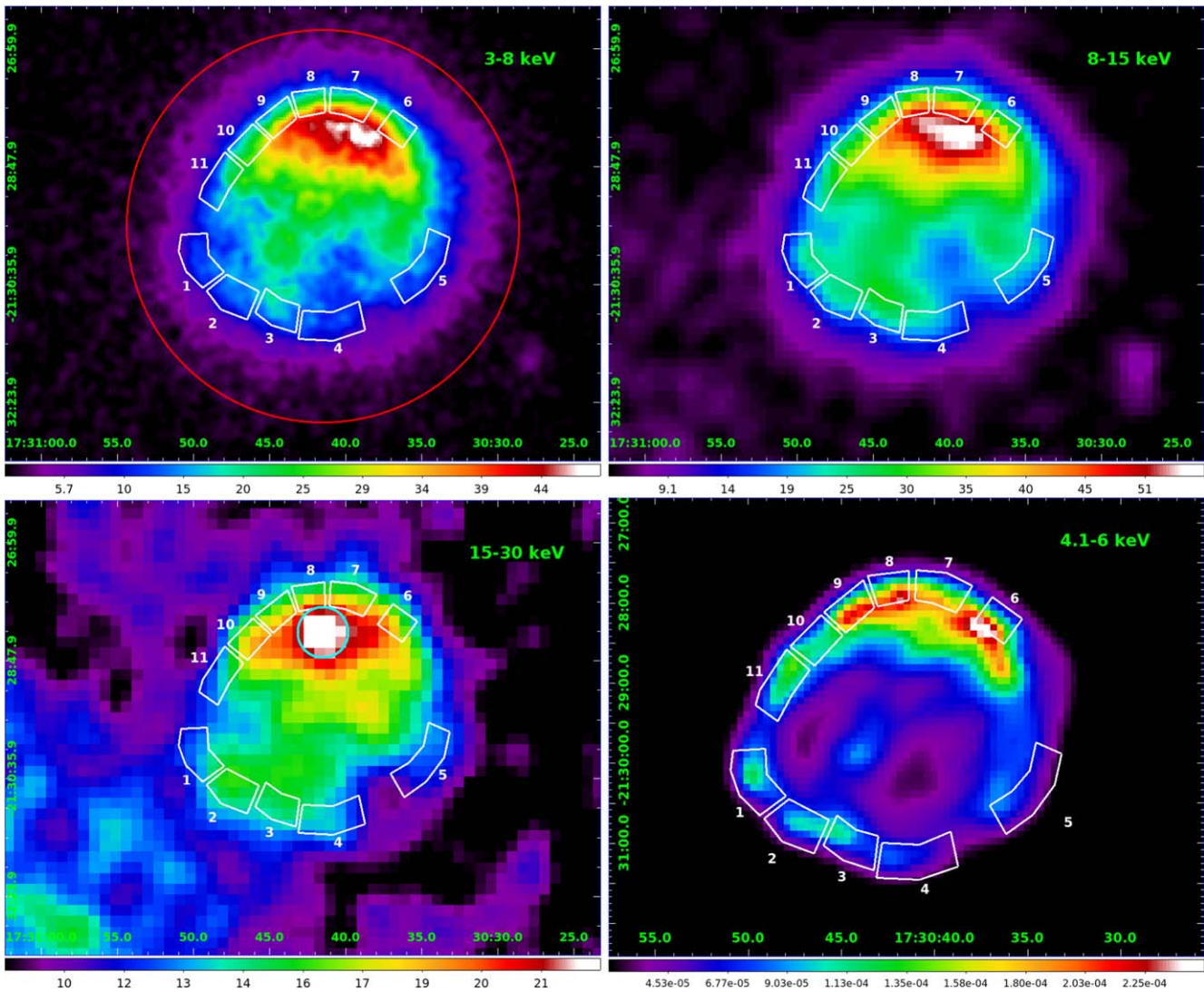[7] http://xmm-tools.cosmos.esa.int/external/xmm_calibration//background/bs_repository/blanksky_all.html

Figure 1. *Upper-left panel:* NuSTAR count image in the 3–8 keV band in linear scale. The bin size is 2″.5, and the image was smoothed through the convolution with a Gaussian with $\sigma = 7″.5$. The red circle marks the extraction region for the total spectrum (see Section 3.2). *Upper-right panel:* NuSTAR count image in the 8–15 keV band in linear scale. The bin size is 7″.5, and the image was smoothed through the convolution with a Gaussian with $\sigma = 22″.5$. *Bottom-left panel:* NuSTAR count image in the 15–30 keV band in linear scale. The bin size is 10″, and the image was smoothed through the convolution with a Gaussian with $\sigma = 30″$. The cyan circle marks the extraction region for the hard X-ray knot (see Section 3.4). Regions selected for the spatially resolved spectral analysis at the rim of the shell are indicated by white polygons. *Bottom-right panel:* XMM-Newton count-rate image in the 4.1–6 keV band in linear scale. The bin size is 5″ and the image was adaptively smoothed to a signal-to-noise ratio of 10. North is up, and east is to the left.

We analyzed the EPIC pn spectra extracted from the same regions adopted for the NuSTAR spectral analysis. To take into account the vignetting effect in the spectra, we added a "weight" column to the pn event file with the `evigweight` SAS command. The spectra were extracted by using the `evselect` task, retaining only events with `FLAG=0` and `PATTERN` $\leqslant 4$. For each spectrum, we produced the RMF and ARF files, with the `rmfgen` and the `arfgen` tasks, respectively. The spectra were rebinned so as to have at least 25 counts per bin. For the background, we selected two extraction regions outside the shell: one, at south, for regions 1–5, and one, at north, for regions 6–11 and for the "Hard Knot" (see Section 3.3 and Figure 1 for the region selection). Spectral analysis of NuSTAR and XMM-Newton data was performed with the HEAsoft software XSPEC version 12.11.1 (Arnaud 1996). The spectra from different cameras were fitted simultaneously.

2.3. Chandra Observation

To study in detail the morphology of the remnant, we also analyzed Chandra observations performed between 2006 April 27 and 2006 August 3 for a total exposure time of 750 ks (Obs. ID: 6714, 6715, 6716, 6717, 6718, 7366; PI: S. Reynolds). The data were reprocessed with the CIAO v4.13 software using CALDB 4.9.4. We reprocessed the data by using the `chandra_repro` task. The mosaicked flux images were obtained by using the `merge_obs` task.

3. Results

3.1. Images

Figure 1 shows the NuSTAR count image in the 3–8 keV, 8–15 keV, and 15–30 keV bands, together with the XMM-Newton count-rate image in the 4.1–6 keV band. The presence

of source photons up to 30 keV confirms the detection of hard X-rays by Nagayoshi et al. (2021). Thanks to the angular resolution of NuSTAR, we can also reveal the spatial distribution of the hard X-ray emission in Kepler's SNR. Figure 1 shows that the morphology of the emission in the 8–15 keV band is roughly similar to the soft X-ray emission, being brighter in the northern part of the shell, where the shock is interacting with the nitrogen-rich CSM. Similarly, in the 15–30 keV band we observe a higher surface brightness in the north than in the south. However, some differences in the morphology of the hard X-ray emission with respect to the soft emission are visible, as, for example, the position of the peak in surface brightness in the 15–30 keV band, which is located to the east with respect to the peak in the 3–8 keV map. We also notice an enhancement in the surface brightness at southeast. The 4.1–6.0 keV XMM-Newton count-rate image is bright in the outermost regions of the remnant, where synchrotron filaments have been spotted (Reynolds et al. 2007). We point out that, because of the higher densities expected in the northern part of the shell, we also expect a larger contribution of thermal bremsstrahlung therein. The high-energy tail of thermal bremsstrahlung can, in principle, contribute to the 15–30 keV emission in the northern part of the shell. However, as we show in Section 3.3, the bulk of the hard X-ray emission of Kepler's SNR has likely a nonthermal origin.

3.2. Total Spectrum

We extracted the spectrum of the whole Kepler's SNR from NuSTAR FPMA and FPMB using a circle with radius of $3'$ and center coordinates $\alpha_{J2000} = 17^h30^m41\overset{s}{.}44$ and $\delta_{J2000} = -21°29'27\overset{''}{.}7$, as shown in Figure 1. We modeled the FPMA and FPMB global spectra in the 4.1–30 keV band. We excluded the 3–4.1 keV band to avoid the strong contamination of thermal emission present in this energy band. We model the hard X-rays as nonthermal emission, by adopting a similar approach as Lopez et al. (2015). However, here we describe the continuum as synchrotron emission from an electron energy distribution limited by radiative losses (hereafter loss-limited model; Zirakashvili & Aharonian 2007), which has been shown to provide an accurate description of nonthermal X-ray emission in young SNRs (e.g., Zirakashvili & Aharonian 2010; Morlino & Caprioli 2012; Miceli et al. 2013; Tsuji et al. 2021). The spectrum of the loss-limited model is given by:

$$\frac{dN_X}{d\varepsilon} \propto \left(\frac{\varepsilon}{\varepsilon_0}\right)^{-2} \left[1 + 0.38\sqrt{\frac{\varepsilon}{\varepsilon_0}}\right]^{\frac{11}{4}} \exp\left(-\sqrt{\frac{\varepsilon}{\varepsilon_0}}\right), \qquad (2)$$

where ε is the photon energy, and ε_0 is the cutoff energy parameter. We include interstellar absorption (Tbabs model in XSPEC), with a hydrogen column density fixed to $N_H = 6.4 \times 10^{21}$ cm^{-2} (as in Katsuda et al. 2015). We also include three ad hoc Doppler-broadened Gaussian components to model the Fe K line (at ∼6.4 keV; see Yang et al. 2013), the Cr and Mn emission lines and the Ni emission lines. Figure 2 shows the total spectra (FPMA and FPMB) of Kepler's SNR with the corresponding best-fit model and residuals. The best-fit values, with error bars at 68% confidence level, are reported in Table 1.

The fit provides $\chi^2/d.o.f. = 1115.82/918$ and an average cutoff energy parameter $\varepsilon_0 = 0.640^{+0.014}_{-0.013}$ keV. This value of ε_0 corresponds to a roll-off frequency $\nu_r = 1.55^{+0.03}_{-0.03} \times 10^{17}$ Hz,
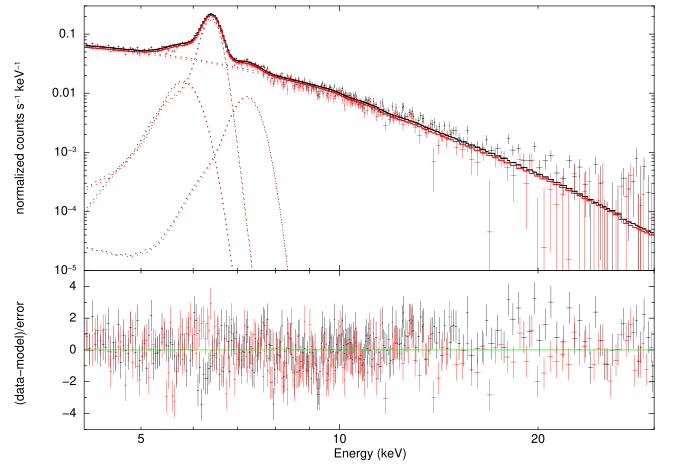

Figure 2. FPMA (black) and FPMB (red) total spectra of Kepler's SNR with the corresponding best-fit model and residual in the 4.1–30 keV band.

Table 1
Best-fit Values for Kepler's SNR NuSTAR Spectra

Parameter	Value
Fe K center (keV)	$6.4018^{+0.0016}_{-0.0014}$
σ (keV)	$0.091^{+0.003}_{-0.003}$
Norm (10^{-4} photons cm^{-2} s^{-1})	$2.96^{+0.02}_{-0.02}$
ε_0 (keV)	$0.640^{+0.014}_{-0.013}$
Norm (10^{-3})	$29.0^{+1.8}_{-1.7}$
$\chi^2/d.o.f.$	1115.82/918

which is in good agreement with the estimate obtained by Nagayoshi et al. (2021; 1×10^{17} Hz) on the basis of the modeling of the broadband SED.

We fitted simultaneously the NuSTAR FPMA and FPMB spectra (in the 4.1–30 keV band), and the Suzaku HXD-PIN spectrum (in the 15–30 keV band), with the loss-limited model. We allowed the normalization of the Suzaku spectra to differ from that of the NuSTAR spectra within a 10% to account for the characteristic cross-calibration factor between the two telescopes (Madsen et al. 2017). We found that the hard X-ray flux of Kepler's SNR in the 15–30 keV band is $1.05^{+0.04}_{-0.03} \times 10^{-12}$ erg cm^{-2} s^{-1} (F_X $1.15^{+0.02}_{-0.24} \times 10^{-12}$ erg cm^{-2} s^{-1} for Suzaku HXD, taking into account the cross-calibration factor). Though this value is lower than that reported by Nagayoshi et al. (2021; $2.75^{+0.78+0.81}_{-0.77-0.82} \times 10^{-12}$ erg cm^{-2} s^{-1}), it is still consistent with it, considering the cross-calibration factor and the 90% statistical and systematic errors.

3.3. Spatially Resolved Spectral Analysis

We performed a spatially resolved spectral analysis by analyzing the spectra extracted from the 11 regions shown in Figure 1. We focus on the outer rim of the shell, by defining regions with similar photon counts in the 8–30 keV band ($N_{8-30} \approx 800$) in order to investigate the relation between the shock velocity and the maximum energy of electrons accelerated at the shock front.

To ascertain the origin of the hard X-ray emission, we first focus on the NuSTAR spectra in the 8–30 keV band. The emission in this band is characterized by a featureless continuum, which can be modeled with a power law with spectral index $\Gamma \sim 3$ in all 11 regions considered. For example,

Table 2
Best-fit Values for Spectra from Regions Labeled from 1 to 11

Region #	Fe K center (keV)	σ (keV)	Norm (10^{-6} photons cm^{-2} s^{-1})	ε_0 (keV)	Norm (10^{-3})	$\chi^2/d.o.f.$
1	$6.445^{+0.019}_{-0.018}$	<0.08	$0.99^{+0.12}_{-0.12}$	$0.57^{+0.07}_{-0.06}$	$0.65^{+0.24}_{-0.18}$	107.08/97
2	$6.38^{+0.04}_{-0.04}$	$0.26^{+0.06}_{-0.05}$	$0.66^{+0.09}_{-0.08}$	$0.47^{+0.05}_{-0.04}$	$0.48^{+0.17}_{-0.13}$	117.76/90
3	$6.427^{+0.018}_{-0.016}$	$0.09^{+0.10}_{-0.02}$	$1.21^{+0.4}_{-0.11}$	$0.43^{+0.04}_{-0.04}$	$1.1^{+0.4}_{-0.3}$	97.02/93
4	$6.395^{+0.016}_{-0.014}$	$0.10^{+0.02}_{-0.02}$	$2.27^{+0.18}_{-0.18}$	$0.48^{+0.05}_{-0.04}$	$1.3^{+0.4}_{-0.3}$	117.52/118
5	$6.410^{+0.009}_{-0.008}$	$0.084^{+0.014}_{-0.014}$	$3.87^{+0.19}_{-0.19}$	$0.54^{+0.06}_{-0.05}$	$0.9^{+0.3}_{-0.2}$	175.24/128
6	$6.441^{+0.007}_{-0.006}$	$0.082^{+0.008}_{-0.008}$	$6.6^{+0.3}_{-0.3}$	$0.50^{+0.05}_{-0.04}$	$1.5^{+0.5}_{-0.4}$	168.34/121
7	$6.448^{+0.005}_{-0.005}$	$0.083^{+0.006}_{-0.007}$	$9.7^{+0.3}_{-0.3}$	$0.59^{+0.06}_{-0.05}$	$1.0^{+0.3}_{-0.3}$	189.15/154
8	$6.443^{+0.006}_{-0.007}$	$0.091^{+0.008}_{-0.008}$	$7.2^{+0.3}_{-0.3}$	$0.67^{+0.09}_{-0.07}$	$0.60^{+0.24}_{-0.17}$	123.26/111
9	$6.434^{+0.005}_{-0.005}$	$0.067^{+0.007}_{-0.007}$	$9.2^{+0.3}_{-0.3}$	$0.64^{+0.08}_{-0.07}$	$0.8^{+0.3}_{-0.2}$	158.83/131
10	$6.419^{-0.006}_{-0.007}$	$0.078^{+0.009}_{-0.009}$	$5.4^{+0.2}_{-0.2}$	$0.59^{+0.07}_{-0.06}$	$0.68^{+0.26}_{-0.19}$	108.60/109
11	$6.404^{+0.012}_{-0.013}$	$0.09^{+0.03}_{-0.02}$	$1.54^{+0.10}_{-0.10}$	$0.59^{+0.06}_{-0.06}$	$0.34^{+0.12}_{-0.09}$	121.37/98
Hard Knot	$6.428^{+0.004}_{-0.003}$	$0.101^{+0.004}_{-0.004}$	$24.8^{+0.6}_{-0.6}$	$0.70^{+0.04}_{-0.04}$	$1.5^{+0.2}_{-0.2}$	466.54/340

Note. All errors are at the 68% confidence level.

in the southern part of the shell, we obtain $\Gamma = 3.5^{+0.5}_{-0.4}$ in region 2 and $\Gamma = 2.7^{+0.3}_{-0.3}$ in region 5; similarly, in the northern limb, $\Gamma = 3.0^{+0.4}_{-0.4}$ in region 7 and $\Gamma = 2.7^{+0.5}_{-0.4}$ in region 10. By modeling this relatively flat emission as thermal Bremsstrahlung, we derive quite high plasma temperatures (namely, $kT = 5.8^{+1.8}_{-1.2}$ keV in region 2, $kT = 9^{+3}_{-2}$ keV in region 5, $kT = 7.8^{+2.8}_{-1.8}$ keV in region 7, and $kT = 10^{+5}_{-3}$ keV in region 10). We then consider the bulk of the hard X-ray emission to be nonthermal. However, we point out that, by including a thermal contribution to the hard X-ray spectra, our conclusions stay unaffected, as shown below.

We then fitted the spectra in the 4.1–30 keV band (4.1–8 keV for EPIC pn and 4.1–30 keV for NuSTAR FPMA and FPMB) using the loss-limited model with an additional Gaussian component to take into account the Fe K line. We also added a further Gaussian component in regions 8–11 to model the Cr/Mn K line detected therein. The spectra from all regions, with the corresponding best-fit model and residual, are shown in Appendix B, Figure 6. The best-fit values for all regions (with the corresponding $\chi^2/d.o.f.$) are shown in Table 2 (error bars are at 68% confidence level).

As a crosscheck, we verified that our assumption on the nonthermal origin of the hard X-ray emission is consistent with the broadband X-ray spectrum. To this end, we fit the spectra of all the regions in the 0.3–30 keV (0.3–8 keV for EPIC pn and 3–30 keV for NuSTAR FPMA and FPMB) by adding thermal components to the loss-limited model derived above.

The soft X-ray spectra (0.3–4.1 keV) for the northern regions show prominent thermal emission features, as the Fe-L line complex in the 0.7–1.2 keV band, and the Si, S, Ar, Ca K lines, respectively at ~1.86, keV ~2.48 keV, ~3.11 keV, and ~3.86 keV. All the spectra are shown in Appendix B, Figure 7, with the corresponding best-fit model and residuals.

The spectra extracted from southern regions (regions 1–5, characterized by a fainter thermal emission) are well described by two components of isothermal optically thin plasma in nonequilibrium of ionization (NEI) with nonsolar abundances and Doppler broadening (`bvrnei` model in XSPEC), in addition to the absorbed loss-limited model (the parameters of the loss-limited model are fixed to the best-fit values shown in Table 2). We also included two Gaussian lines to take into account missing Fe-L lines in the `bvrnei` model (as in

Katsuda et al. 2015). The spectra extracted from northern regions (regions 6–11, characterized by a brighter thermal emission) were fitted by adding three thermal components to the loss-limited model (with parameters fixed to the values in Table 2). We found a degeneracy between the Fe abundance, the normalization and the temperature (kT_h) of the hottest component of the plasma. Nagayoshi et al. (2021) found $kT_h = 3.74^{+0.12}_{-0.03}$ keV so we decided to set an upper limit of 4 keV for kT_h. The values of the best-fit parameters are listed in Tables 3 and 4. This model provides a good description of the spectra of all regions ($1 < \chi^2/d.o.f. < 1.4$). We conclude that the modeling of the synchrotron emission adopted in the analysis of the "hard" spectra is consistent with the broadband X-ray spectra and provides a robust description of the nonthermal emission in Kepler's SNR.

3.4. Hard X-Ray Knot

Lastly, we analyzed the spectrum of the knot with the brightest hard X-ray emission, which we spotted in the 15–30 keV band map of Kepler's SNR. In particular, we extracted the EPIC pn, FPMA, and FPMB spectra from the circular region indicated by the cyan circle in the lower left panel of Figure 1.

We modeled the spectra in the the 4.1–30 keV band (4.1–8 keV for EPIC pn and 4.1–30 keV for NuSTAR FPMA and FPMB) by adopting the loss-limited model (with the additional Gaussian component) described in detail in Section 3.3. Spectra from the hard knot, with the corresponding best-fit model and residual, are shown in Figure 3, while the best-fit values (with errors at the 68% confidence level) are shown in Table 2.

4. Discussion

4.1. Different Regimes of Particle Acceleration in Kepler's SNR

The cutoff energy parameter ε_0 is a crucial factor in order to characterize the acceleration mechanism in SNRs, because it is determined by the balance between acceleration and cooling in the synchrotron emission process. Zirakashvili & Aharonian (2007) derived a relation between ε_0, the Bohm factor, and the
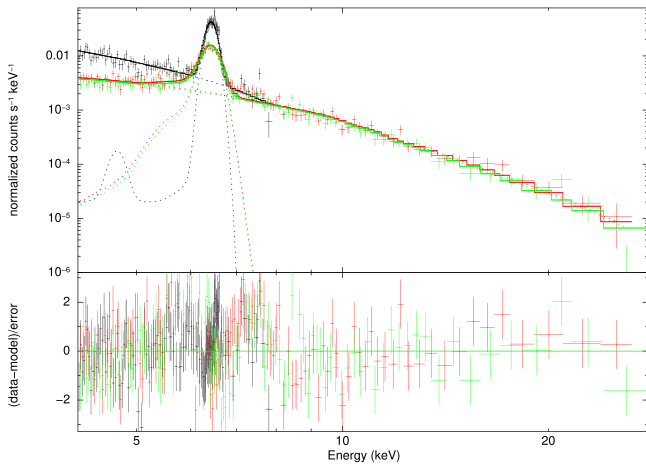
Figure 3. EPIC pn (black), FPMA (red), and FPMB (green) spectra of the hardest knot in Kepler's SNR (cyan circle in Figure 1) with the corresponding best-fit model and residual in the 4.1–30 keV band.

shock velocity,

$$\varepsilon_0 = \frac{1.6}{\eta} \left(\frac{v_{\text{sh}}}{4000 \ \text{km s}^{-1}} \right)^2 \text{keV}. \quad (3)$$

By adopting the same approach as Tsuji et al. (2021), we show in the left panel of Figure 4 the values of ε_0 obtained from the spectral fittings of the regions with a proper-motion measurement available either in Katsuda et al. (2008) or in Coffin et al. (2022), as a function of the corresponding v_{sh}. We mark with different colors data points derived for southern regions (black) and northern regions (red). In northern regions we obtain, on average, lower shock velocities and higher ε_0 values than in southern regions ($\varepsilon_0^S = 0.48 \pm 0.02$ keV, $\varepsilon_0^N = 0.60 \pm 0.03$ keV, for regions 2–5 and regions 6–9/11, respectively). Moreover, the figure shows that southern and northern regions identify two distinct clusters. This suggests the presence of two different regimes of electron acceleration in the same SNR. If we describe each of the two clusters with Equation (3), we can derive the corresponding best-fit values of the Bohm diffusing factor, obtaining $\eta = 6.6 \pm 1.6$ in the north and reaching the Bohm limit in the south. These values are similar to those derived by Tsuji et al. (2021), who find $\eta \sim 0.3$–4. However, Tsuji et al. (2021) adopted a distance of 4 kpc (instead of 5 kpc) to derive the shock velocity from the proper-motion measurements, thus obtaining lower velocities than those reported in the left panel of Figure 4, which is in line with their lower values of η.

Taking into account these results, we can estimate the acceleration time of electrons (Malkov & Drury 2001; Vink 2020) as

$$t_{\text{acc}} \approx 756 \frac{\eta}{\delta} \sqrt{\frac{\varepsilon_0}{1 \ \text{keV}}} \left(\frac{v_{\text{sh}}}{5000 \ \text{km s}^{-1}} \right)^{-2} \left(\frac{B}{10 \ \mu\text{G}} \right)^{-\frac{3}{2}} \text{yr}, \quad (4)$$

where δ accounts for the energy dependence of the diffusion coefficient, and typically ranges between 0.3 and 0.7 (see Strong et al. 2007). Considering $\delta = 0.5$ and taking the values we found in the northern shell ($v_{\text{sh}} = 1800$ km s^{-1}, $\eta = 1$ and $\varepsilon_0 = 0.64$ keV), we derive $t_{\text{acc}} \approx 300 \cdot \left(\frac{B}{100\mu\text{G}} \right)^{-\frac{3}{2}}$ yr. Such a high value of the acceleration time may suggest that the electrons started to accelerate before the interaction of the

shock with the CSM, which produced a deceleration of the northern shock front. Aharonian & Atoyan (1999) suggested that the shock velocity should be larger than 2000 km s^{-1} to emit synchrotron X-rays (see also Vink 2008). Thus the existence of synchrotron X-rays implies that the deceleration should happen recently. Similar situation happens in a superbubble with synchrotron X-rays, 30 Dor C (Bamba et al. 2004), where the supernova shock just hit the shell of the superbubble and emit synchrotron X-rays (Yamaguchi et al. 2009) although Lopez et al. (2020) suggests the superbubble itself accelerate electrons.

In this framework, the current shock velocity may not be representative of the shock conditions over the whole acceleration process. We then explore an alternative scenario, by studying the relationship between the synchrotron cutoff energy and the average shock velocity, $\overline{v_{\text{sh}}}$ in all the regions selected for our spatially resolved spectral analysis. We derived $\overline{v_{\text{sh}}}$ for each region as $\overline{v_{\text{sh}}} = r_{\text{sh}}/t_{\text{age}}$, where r_{sh} is the radius of the shock. We estimated r_{sh} for regions 1–11 by measuring the distance between the shock front and the center of the remnant (whose position was carefully derived by Sato & Hughes 2017). The measuring procedure was performed detecting the edge at the azimuthal center of each region on the Chandra flux image in the 4.1–6 keV band, to exploit the high spatial resolution of the Chandra mirrors (we associated to the angular distance an error of 1".5).

Figure 4 (*right panel*) shows the values of ε_0 obtained from the spectral fittings of the 11 regions analyzed as a function of the corresponding $\overline{v_{\text{sh}}}$. Again, in northern regions we obtain, on average, lower shock velocities and higher ε_0 values than in southern regions ($\varepsilon_0^S = 0.48 \pm 0.02$ keV, $\varepsilon_0^N = 0.59 \pm 0.02$ keV, for regions 1–5 and regions 6–11, respectively). Moreover, also in this plot, southern and northern regions clearly identify two distinct clusters. Therefore, by adopting the average shock velocities, we recover the presence of two different regimes of electron acceleration in the Kepler's SNR. Each of the two clusters can be well described by Equation (3) with a specific value of η. We then derive the corresponding best-fit values of the Bohm diffusing factor, obtaining $\eta = 9.3 \pm 0.4$ in the north and $\eta = 6.2 \pm 0.2$ in the south, with a null hypothesis probability of $\sim 90\%$. These values of η are higher than those derived with the current shock velocities. This is because the deceleration of the shock front makes the current velocities systematically lower than the average velocities (see Equation (3) for the dependence of η on v_{sh}). Therefore, the values of the Bohm factors should be taken with some caution.

The two scenarios considered above, namely, synchrotron emission originating from (i) electrons accelerated in the current shock conditions (i.e., freshly accelerated electrons in a high magnetic field), and (ii) electrons accelerated well before the interaction with the dense CSM at north (i.e., longer acceleration times, possibly associated with a lower magnetic field, as in Nagayoshi et al. 2021), may be considered as two limiting cases, bracketing the actual evolution of the system.

Nevertheless, regardless of the shock velocity adopted (current velocity versus average velocity), our conclusions do not change, as both the plots shown in Figure 4 point toward a more efficient (i.e., closer to the Bohm limit) electron acceleration in the north than in the south.

On the other hand, a scenario in which ε_0 does not depend on the shock velocity is also possible. We tested this possibility by
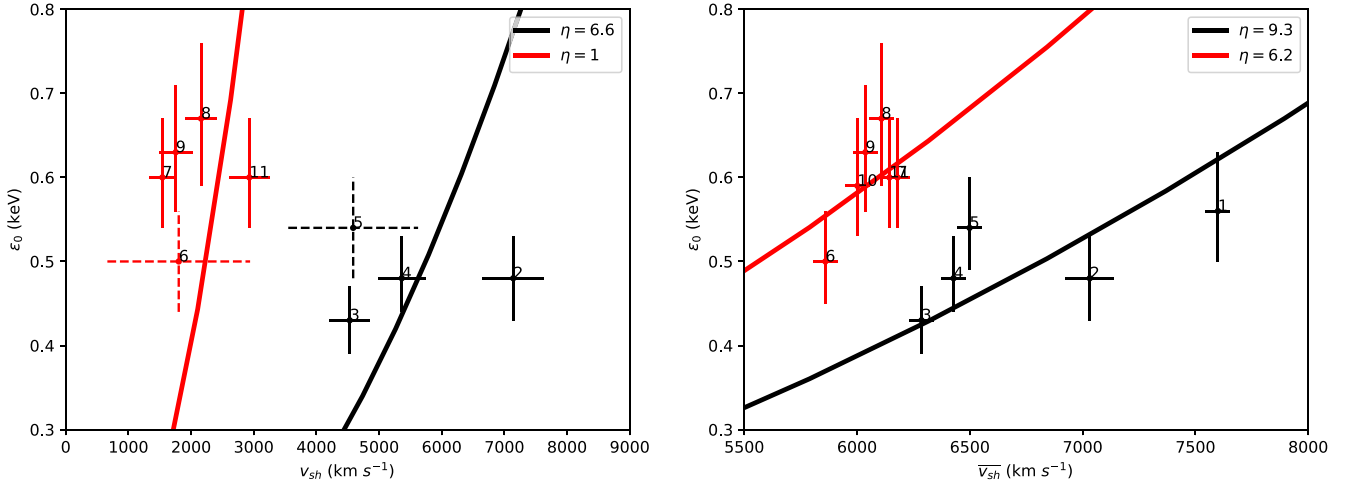
Figure 4. *Left panel:* Synchrotron cutoff energy vs. current shock velocity derived from Coffin et al. (2022; solid crosses) and Katsuda et al. (2008; dashed crosses, see Appendix C for details). Red crosses mark northern regions (6–9/11), and the red solid curve is the corresponding best-fit curve obtained from Equation (3). Black crosses mark southern regions (2–5), and the black solid curve is the corresponding best-fit curve obtained from Equation (3). *Right panel:* Synchrotron cutoff energy vs. average shock speed for Kepler's SNR. Red crosses mark regions 6–11, and the red solid curve is the corresponding best-fit curve obtained from Equation (3). Black crosses mark regions 1–5, and the black solid curve is the corresponding best-fit curve obtained from Equation (3).
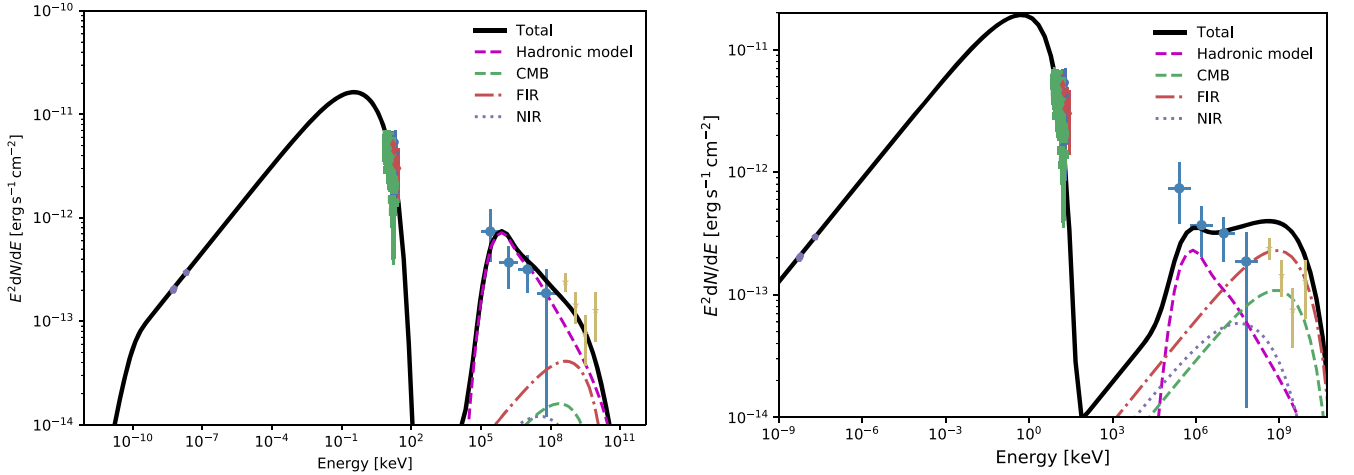

Figure 5. *Left panel:* SED of Kepler's SNR. Radio data (violet) are from DeLaney et al. (2002), NuSTAR (FPMA and FPMB, blue and green, respectively) X-ray data are extracted from the whole remnant, HXD-PIN X-ray data (dark red) are from Nagayoshi et al. (2021), GeV γ-ray data (steel blue) are from Acero et al. (2022), and TeV γ-ray data (yellow) are from Prokhorov et al. (2022). The black curve indicates our combined leptohadronic model, including contributions from π^0 decay (dashed magenta curve), and inverse Compton emission from the cosmic microwave background (green dashed curve), far-infrared (red, dashed–dotted curve), and near-infrared emission (purple dotted curve). In the leptohadronic model, the magnetic field is 100 μG, and the post-shock density is 20 cm^{-3}. *Right panel:* Same as left panel but with a magnetic field of 40 μG and a post-shock density of 5 cm^{-3}.

fitting the data points of Figure 4 with a constant ε_0 and obtained a null hypothesis probability of $\sim$15%, which is well below the value obtained in the loss-limited case but still statistically acceptable. However, a framework where ε_0 does not depend on $v_{\rm sh}$ would indicate that the maximum electron energy is not limited by radiative losses, and, as explained in Section 1, this would imply a magnetic field lower than 30 μG (assuming $\varepsilon_0 = 0.5$ keV), which is at odds with the observations (Völk et al. 2005; Parizot et al. 2006; Rettig & Pohl 2012; Reynolds et al. 2021).

The cutoff energies discussed above were obtained by assuming that the X-ray continuum above 4 keV is ascribed to synchrotron radiation. We then checked how a possible contamination of thermal emission in the hard X-ray spectra of northern regions (where thermal emission is the highest) affects our results. We found that if we model the hard continuum of regions 6–11 with a combination of synchrotron

radiation and thermal Bremsstrahlung, the value of ε_0 systematically increases with the contribution of thermal emission. The values of ε_0 for regions 6–11 shown in Table 2 and Figure 4 should then be considered as lower limits. This means that the acceleration efficiency in the north may be even higher (and the Bohm diffusing factor lower) than that derived by neglecting the contribution of thermal emission to the hard X-ray continuum. We conclude that the evidence of more efficient acceleration in the northern part of Kepler's SNR is solid. Southern regions, where the thermal emission has a lower surface brightness, are less affected by thermal contamination and the synchrotron component is better constrained. We note that Tsuji et al. (2021) finds small-scale variations in ε_0, with local peaks reaching values of the order of 1.5 keV (higher than those reported in our Table 2). This may be due to the absence of NuSTAR data for Kepler's SNR in Tsuji et al. (2021) and to

the different size of the extraction regions (our regions being significantly larger than theirs).

We note that in the southern part of Kepler's SNR, where the ambient density is similar to that observed in Tycho's SNR (Blair et al. 2007), we recover similar results as those obtained for Tycho's SNR by Lopez et al. (2015), who found that the cutoff energy increases with the shock velocity (i.e., where the ambient density is low). At odds with Tycho's SNR, however, Kepler's SNR is interacting with a much denser environment in the north (4–7 times denser; Blair et al. 2007; Katsuda et al. 2008), where we register a different regime of particle acceleration.

The presence of two different acceleration regimes and of a higher acceleration efficiency in regions 6–11 might be explained by considering the turbulent magnetic field generated in the interaction between the shock front and the dense CSM in the north. Inoue et al. (2012) modeling RX J1713.7–3946 SNR with a 3D magnetohydrodynamic (MHD) simulation show that a shock wave that sweeps a cloudy medium generates an amplified magnetic field, as a result of the dynamo action induced by the turbulent shock-cloud interaction (See also Orlando et al. 2008). An amplified magnetic field may lead toward a more efficient acceleration process and to a lower η Bohm factor. This interpretation is in line with the findings obtained for RX J1713.7-3946 by Sano et al. (2015), who observed that the synchrotron photon index is anticorrelated with the X-ray intensity. Indeed, we found the highest value of ε_0 in the "Hard Knot" region, which we identified in the northern part of the shell as a bright feature in the 15–30 keV map (see Figure 1 and Table 2). In general, our findings show that in Kepler's SNR the ε_0 parameter is high in the region where the shock interacts with high-density CSM, thus indicating a similar scenario as that proposed for RX J1713.7–3946.

4.2. Spectral Energy Distribution

Several SNRs are known to emit γ-rays up to TeV energy (e.g., Ackermann et al. 2013; HESS Collaboration et al. 2018; Aleksić et al. 2012). Xiang & Jiang (2021) reported a likely detection (with ~4σ significance) of γ-ray emission in the 0.2–500 GeV band from the region of Kepler's SNR by analyzing Fermi Large Area Telescope (LAT) data. Using the same Fermi LAT data, Acero et al. (2022) confirmed this detection up to 6σ. Moreover, Prokhorov et al. (2022) reported the detection of VHE emission from Kepler's SNR based on a deep observation of HESS.

In this section, we model the SED of Kepler's SNR for the nonthermal emission, using radio (DeLaney et al. 2002), X-ray (NuSTAR FPMA and FPMB in the 8–30 keV band from this work and HXD-PIN from Nagayoshi et al. 2021), GeV (Xiang & Jiang 2021), and TeV (Prokhorov et al. 2022) data, and give some constraints on the particle energy distribution and on the ambient density and magnetic field.

We use the radiative code `naima` (version 0.9.1, Zabalza 2015) to model the SED. We considered a leptohadronic one-zone stationary model to describe the multiband emission spectrum. In this model, the synchrotron and inverse Compton (IC) emission are assumed to stem from the same electron distribution, which is described by a power law with an exponential cutoff. We considered the same seed photon field as Nagayoshi et al. (2021) for the IC emission: the cosmic microwave background radiation (CMBR), a far-infrared (FIR)

component ($T = 29.5$ K and $u_{\mathrm{FIR}} = 1.08$ eV cm^{-3}), and a near-infrared (NIR) component ($T = 1800$ K and $u_{\mathrm{NIR}} = 2.25$ eV cm^{-3}). As for the hadrons, we assumed a power-law energy distribution with an exponential cutoff. The model that best reproduces the observed data is shown in Figure 5 (left panel).

Our model gives for the leptonic part a spectral index $\alpha = 2.44$ and a cutoff energy $E_{\mathrm{cut}} = 16$ TeV. The electrons emit synchrotron radiation in a magnetic field of 100 μG. For the hadronic part we assumed the same spectral index and an energy cutoff of 500 TeV. The total kinetic energy of protons (W_p), interacting with a post-shock medium with density of 20 cm^{-3} (consistent with the density value of the shock–CSM interacting region; Kasuga et al. 2021), was set to be 15 times the electrons total kinetic energy ($W_p = 4.2 \times 10^{48}$ erg). As a comparison we also modeled the SED using the value for the magnetic field proposed by Nagayoshi et al. (2021; B=40 μG, see Figure 5 right panel), with $\alpha = 2.44$ and $E_{\mathrm{cut}} = 35$ TeV for the leptonic part. For the hadronic part of the model we adopted the same assumption as before but with $W_p = 5.4 \times 10^{48}$ erg (4 times the electrons total kinetic energy) and a post-shock medium density of 5 cm^{-3}. This last case gives a poor fit compared with the case where the magnetic field is higher.

5. Conclusions

We analyzed an archive NuSTAR observation of Kepler's SNR. We detected hard X-ray emission up to ~30 keV, mainly stemming from the northern part of the remnant, where the shock front is interacting with dense circumstellar material. We verified that the bulk of the hard X-ray emission is nonthermal and performed a spatially resolved spectral analysis focusing on the outer rim of the shell by combining NuSTAR and XMM-Newton spectra. We adopted the loss-limited synchrotron emission model by Zirakashvili & Aharonian (2007) to determine the cutoff photon energy parameter in 11 regions. We identified two different acceleration regimes in the northern and southern limbs of Kepler's SNR. In particular, we found lower Bohm factors (i.e., more efficient electron acceleration) in the northern part of the shell than in the south. We suggest that the interaction of the shock front with the high-density CSM at north generates an amplified, possibly turbulent, magnetic field, which facilitates the particle acceleration process.

An alternative scenario of constant cutoff energy across the shell of Kepler's SNR is disfavoured by our analysis. This would imply that the maximum electron energy is not limited by radiative losses (which would require that the magnetic field is much smaller than that observed), though it cannot be statistically excluded.

We produced the spectral energy distribution including also NuSTAR X-ray data. We were able to reproduce all the data with a leptohadronic model with a magnetic field of 100 μG, a medium density of 20 cm^{-3}, electron energy $W_e = 2.7 \times 10^{47}$ erg, and proton energy $W_p = 4.2 \times 10^{48}$ erg. The density we found in modeling the SED is consistent with that derived in the northern region by Kasuga et al. (2021), suggesting a scenario in which the majority of the hadronic emission originates in the northern part of the remnant. The bright nonthermal hard X-ray emission that we detected in the northern half of Kepler's SNR strongly suggests that this region is also a site of leptonic emission.

Software: NuSTARDAS (v2.0.0), HEAsoft (v6.28; HEA-SARC 2014), SAS (v18.0.0; Gabriel et al. 2004), XSPEC (v12.11.1; Arnaud 1996), CIAO (v4.13; Fruscione et al. 2006), naima (v0.9.1, Zabalza 2015).

Appendix A
Best-fit Values for Broadband Spectra

The best-fit values for the spectra of southern regions, using a model with two thermal components plus the loss limited model, are shown in Table 3. The best-fit values for the spectra of northern regions, using a model with three thermal components plus the loss limited model, are shown in Table 4.

Table 3
Best-fit Values for Broadband Spectra of Southern Regions (1–5)

Component	Parameter	#1	#2	#3	#4	#5
TBabs	n_H (10^{22} cm^{-2})			0.64 (fixed)		
Gauss$_1$	Fe L + O K (keV)			0.708 (fixed)		
	Norm (10^{-4} photons cm^{-2} s^{-1})	$2.8^{+0.6}_{-0.7}$	$1.7^{+0.7}_{-0.7}$	$4.3^{+0.9}_{-0.9}$	$11.0^{+1.3}_{-1.2}$	$11.6^{+1.3}_{-2.1}$
Gauss$_2$	Fe L+Ne K (keV)			1.227 (fixed)		
	Norm (10^{-4} photons cm^{-2} s^{-1})	$0.053^{+0.017}_{-0.014}$	$0.026^{+0.014}_{-0.014}$	$0.051^{+0.016}_{-0.016}$	$0.14^{+0.02}_{-0.02}$	$0.15^{+0.03}_{-0.02}$
brvnei$_1$	kT$_1$ (keV)	$0.63^{+0.09}_{-0.05}$	$0.65^{0.11}_{-0.09}$	$0.54^{+0.06}_{-0.06}$	$0.68^{+0.03}_{-0.07}$	$0.721^{+0.007}_{-0.073}$
	O	1(fixed)	$1.5^{+1.0}_{0.9}$	$2.2^{+0.3}_{-0.6}$	$0.31^{+0.18}_{-0.17}$	1 (fixed)
	Ne	1 (fixed)	$1.3^{+1.1}_{-0.9}$	1 (fixed)	<0.5	1 (fixed)
	Mg	1 (fixed)	6^{+4}_{-3}	$4.80485^{+1.7}_{-1.4}$	$0.9^{+0.5}_{-0.5}$	$4.3^{+0.8}_{-0.7}$
	Si		1 (fixed)		$9.0^{+1.9}_{-1.8}$	1 (fixed)
	Fe	19^{+5}_{-3}	81^{+18}_{-15}	51^{+12}_{-7}	50^{+4}_{-5}	107^{+4}_{-5}
	τ_1 (10^9 cm^{-3} s)	<0.6	$1.05^{+0.14}_{-0.13}$	<0.62	$0.83^{+0.07}_{-0.12}$	$1.20^{+0.04}_{-0.03}$
	Velocity (10^4 km s^{-1})	0	$0.7^{+0.3}_{-0.5}$	0	0	$0.64^{+0.07}_{-0.10}$
	EM$_1$ (10^{56} cm^{-3})	$2.9^{+0.4}_{-0.8}$	$0.62^{+0.20}_{-0.14}$	$2.4^{+0.7}_{-0.8}$	$4.6^{+1.1}_{-0.4}$	$4.16^{+0.10}_{-0.27}$
brvnei$_2$	kT$_2$ (keV)	>3.88	>3.89	>3.93	>3.91	>3.95
	O	1 (fixed)	<2.5	<1.7	5^{+3}_{-2}	1 (fixed)
	Ne	$3.7^{+5.3}_{-1.4}$	$2.4^{+1.2}_{-1.0}$	$4.2^{1.3}_{-0.8}$	$5.2^{+2.1}_{-1.3}$	23^{+10}_{-3}
	Mg	5^{+7}_{-2}	$1.2^{+0.9}_{-0.8}$	$1.2^{+0.7}_{-0.5}$	$2.3^{1.0}_{-0.7}$	$14.0^{+1.3}_{-3.0}$
	Si	$45^{+64}_{-1.7}$	20^{+6}_{-4}	30^{+10}_{-6}	37^{+14}_{-8}	170^{+720}_{-40}
	S	50^{+80}_{-20}	23^{+9}_{-6}	38^{14}_{-9}	48^{+19}_{-11}	300^{+700}_{-40}
	Ar	50^{+100}_{-40}	26^{+24}_{-19}	40^{+30}_{-20}	36^{+25}_{-17}	180^{+40}_{-50}
	Ca		1 (fixed)		24^{+30}_{-22}	110^{+70}_{-80}
	Fe	27^{+3}_{-2}	$13.8^{1.2}_{-1.1}$	$21.5^{+1.3}_{-1.2}$	$26.8^{+1.1}_{-1.3}$	$43.5^{+0.7}_{-1.7}$
	Ni			=Fe		
	τ_2 (10^9 cm^{-3} s)	$4.51^{+2.3}_{0.17}$	$5.3^{+0.3}_{-0.2}$	$4.65^{+0.14}_{-0.12}$	$5.12^{+0.13}_{-0.13}$	$7.14^{+0.10}_{-0.07}$
	Velocity (10^4 km s^{-1})	$0.58^{+0.09}_{-0.09}$	$0.738^{+0.09}_{-0.10}$	$0.42^{+0.06}_{-0.07}$	$0.42^{+0.05}_{-0.05}$	$0.57^{0.02}_{-0.03}$
	EM$_2$ (10^{56} cm^{-3})	$1.959^{+0.003}_{-0.004}$	$0.050^{+0.004}_{-0.004}$	$0.074^{+0.003}_{-0.004}$	$0.113^{+0.007}_{-0.006}$	$0.095^{+0.006}_{-0.007}$
	$\chi^2/d.o.f.$	458.98/456	403.14/355	423.15/443	608.79/573	824.00/626

Note. Solar abundances from Anders & Grevesse (1989). The τ lower limit is set to be 5×10^8 cm^{-3} s. The abundance upper limit is set to be 1000 times the solar one. The velocity upper limit is set to be 1×10^4 m s^{-1}. Abundances consistent with their solar values were fixed to 1.

Table 4
Best-fit Values for Broadband Spectra of Northern Regions (6–11)

Component	Parameter	#6	#7	#8	#9	#10	#11
TBabs	n_H (10^{22} cm^{-2})			0.64 (fixed)			
Gauss$_1$	Fe L + O K (keV)			0.708 (fixed)			
	Norm (10^{-4} photons cm^{-2} s^{-1})	$18.5^{+1.7}_{-1.8}$	$17.16^{+0.15}_{-0.15}$	$8.6^{+1.3}_{-1.3}$	$25.2^{+1.7}_{-1.5}$	$22.1^{+1.2}_{-1.4}$	$5.9^{+1.2}_{-0.7}$
Gauss$_2$	Fe L+Ne K (keV)			1.227 (fixed)			
	Norm (10^{-4} photons cm^{-2} s^{-1})	$0.83^{+0.07}_{-0.05}$	$1.413^{+0.06}_{-0.06}$	$1.02^{+0.05}_{-0.05}$	$1.18^{+0.06}_{-0.06}$	$0.584099^{+0.04}_{-0.04}$	$0.23^{+0.02}_{-0.02}$
Gauss$_3$	Cr K+Mn K (keV)			5.6 (fixed)			
	Norm (10^{-4} photons cm^{-2} s^{-1})	/	/	$0.003^{+0.002}_{-0.002}$	$0.006^{+0.002}_{-0.002}$	$0.0024^{+0.0017}_{-0.0016}$	$0.0029^{+0.0009}_{-0.0009}$
brvnei$_1$	kT$_1$ (keV)	$0.409^{+0.011}_{-0.017}$	$0.431^{+0.006}_{-0.013}$	$0.442^{+0.015}_{-0.013}$	$0.430^{+0.007}_{-0.008}$	$0.341519^{+0.013}_{-0.014}$	$0.389980^{+0.04}_{-0.02}$
	C	$2.0^{+0.9}_{-0.9}$	$7.8^{+3.0}_{-1.8}$	11^{+6}_{-3}	$7.0^{+2.3}_{-1.7}$	31^{+6}_{-6}	<7
	N			0 (fixed)			
	O	$0.41^{+0.05}_{-0.04}$	$0.58^{+0.16}_{-0.09}$	$0.90^{+0.4}_{-0.2}$	$0.68^{+0.14}_{-0.10}$	$1.40^{+0.15}_{-0.15}$	$0.34^{+0.12}_{-0.09}$
	Ne	$4.1^{+0.4}_{-0.4}$	$7.1^{+1.8}_{-1.0}$	$6.6^{+2.6}_{-1.3}$	$6.1^{+1.1}_{-0.8}$	$12.8^{+1.7}_{-1.7}$	$2.9^{+0.9}_{-0.5}$
	Mg	$5.0^{+0.7}_{-0.6}$	$12.3^{3.1}_{-1.7}$	10^{+4}_{-2}	$11.6^{+2.1}_{-1.3}$	29^{+4}_{-4}	1(fixed)
	Fe	$51.4^{1.4}_{-5.7}$	93^{+27}_{-15}	100^{+40}_{-20}	109^{+22}_{-16}	275^{+12}_{-9}	70^{+24}_{-15}
	Ni			=Fe			
	τ_1 (10^9 cm^{-3} s)	$1.23^{+0.06}_{-0.07}$	$1.41^{+0.05}_{-0.04}$	$1.50^{+0.06}_{-0.05}$	$1.30^{+0.03}_{-0.03}$	$0.993^{+0.05}_{-0.04}$	$1.08^{+0.07}_{-0.07}$
	Velocity (10^4 km s^{-1})	>0.74	$0.55^{+0.05}_{-0.05}$	0 (fixed)	$0.60^{+0.05}_{-0.05}$	$0.36^{+0.11}_{-0.13}$	$0.65^{+0.17}_{-0.16}$
	EM$_1$ (10^{56} cm^{-3})	32^{+4}_{-3}	16^{+3}_{-4}	8^{+2}_{-2}	18^{+3}_{-3}	$7.5^{+0.3}_{-0.3}$	$7.4^{+1.8}_{-1.8}$
brvnei$_2$	kT$_2$ (keV)	$0.97^{+0.06}_{-0.05}$	$1.32^{+0.06}_{-0.06}$	$1.43^{0.07}_{-0.06}$	$1.23^{+0.06}_{-0.04}$	$1.15^{+0.06}_{-0.03}$	$1.50^{+0.20}_{-0.16}$
	O	42^{+10}_{-9}	20^{+7}_{-6}	27^{+10}_{-8}	33^{+10}_{-9}	11.2175^{+2}_{-2}	30^{+26}_{-26}
	Ne	46^{+10}_{-9}	1 (fixed)		40^{+9}_{-10}	9.00606^{+3}_{-2}	22^{+16}_{-21}
	Mg	58^{+11}_{-12}	61^{+8}_{-10}	72^{+14}_{-17}	69^{+12}_{-15}	$18.4^{+2.2}_{-1.8}$	46^{+16}_{-40}
	Si	180^{+30}_{-60}	230^{+30}_{-40}	270^{+50}_{-70}	280^{+50}_{-50}	114^{+11}_{-9}	300^{+100}_{-270}
	S	290^{+60}_{-90}	380^{+50}_{-60}	470^{+80}_{-90}	480^{+90}_{-90}	183^{+18}_{-16}	450^{+160}_{-390}
	Ar	350^{+100}_{-90}	370^{+80}_{-70}	520^{+110}_{-140}	520^{+130}_{-140}	240^{+30}_{-30}	250^{+240}_{-220}
	Ca	>600	>800	>700	>800	360^{+90}_{-80}	>100
	Fe	28^{+6}_{-6}	69^{+9}_{-12}	90^{+17}_{-23}	70^{+11}_{-18}	$24.8^{+2.4}_{-0.8}$	1 (fixed)
	Ni			=Fe			
	τ_2 (10^9 cm^{-3} s)	57^{+6}_{-6}	43^{+3}_{-3}	36^{+2}_{-2}	$39.9^{+1.8}_{-2.8}$	$38.0^{+1.1}_{-4.4}$	32^{+6}_{-5}
	Velocity (10^4 km s^{-1})	$0.394^{+0.017}_{-0.017}$	$0.533^{+0.014}_{-0.014}$	$0.438^{+0.016}_{-0.015}$	$0.39^{+0.05}_{-0.05}$	$0.480^{+0.014}_{-0.014}$	$0.48^{+0.03}_{-0.04}$
	EM$_2$ (10^{56} cm^{-3})	$0.121^{+0.003}_{-0.010}$	$0.074^{+0.016}_{-0.008}$	$0.044^{+0.015}_{-0.007}$	$0.068^{+0.022}_{-0.011}$	$0.140^{+0.012}_{-0.012}$	$0.011^{+0.079}_{-0.003}$
brvnei$_3$	kT$_3$ (keV)	>3.91	>3.98	>3.97	>3.95	>3.96	>3.88
	Ne	40^{+30}_{-30}	1 (fixed)				
	Si	1 (fixed)		<50	1 (fixed)		28^{+146}_{-17}
	S	134^{+134}_{-133}	1 (fixed)				
	Ar	600^{+400}_{-400}	lt500	1 (fixed)	lt500	1 (fixed)	
	Ca	1 (fixed)					190^{+470}_{-110}
	Fe	>900	>800	>800	>900	>970	190^{+720}_{-80}
	Ni			=Fe			
	τ_3 (10^9 cm^{-3} s)	$6.49^{0.18}_{0.22}$	$6.78^{+0.12}_{-0.11}$	$6.32^{+0.12}_{-0.11}$	$6.50^{+0.09}_{-0.11}$	$6.31^{+0.13}_{-0.13}$	$6.49^{+0.19}_{-0.21}$
	Velocity (10^4 km s^{-1})	$0.59^{+0.06}_{-0.06}$	$0.53^{+0.04}_{-0.04}$	$0.59^{+0.05}_{-0.05}$	$0.43^{+0.05}_{-0.05}$	$10.51^{+0.06}_{-0.06}$	>0.9
	EM$_3$ (10^{56} cm^{-3})	$0.0100^{+0.0006}_{-0.0004}$	$0.0134^{+0.0027}_{-0.0002}$	$0.0099^{+0.0032}_{-0.0002}$	$0.0137^{+0.0024}_{-0.0002}$	$0.0078^{+0.0002}_{-0.0002}$	$0.014^{+0.008}_{-0.011}$
	$\chi^2/d.o.f.$	834.12/662	927.60/713	748.64/644	860.19/681	7748.25/628	545.85/494

Note. Solar abundances from Anders & Grevesse (1989). The τ lower limit is set to be 5×10^8 cm^{-3} s. The abundance upper limit is set to be 1000 times the solar one. The velocity upper limit is set to be 1×10^4 m s^{-1}. Abundances consistent with their solar values were fixed to 1.

Appendix B
Spectra

In Figures 6 and 7 are shown, respectively, the spectra extracted for regions 1–11 in the 4.1–30 keV band and in the 0.3–30 keV band, with the corresponding best-fit model and residuals.
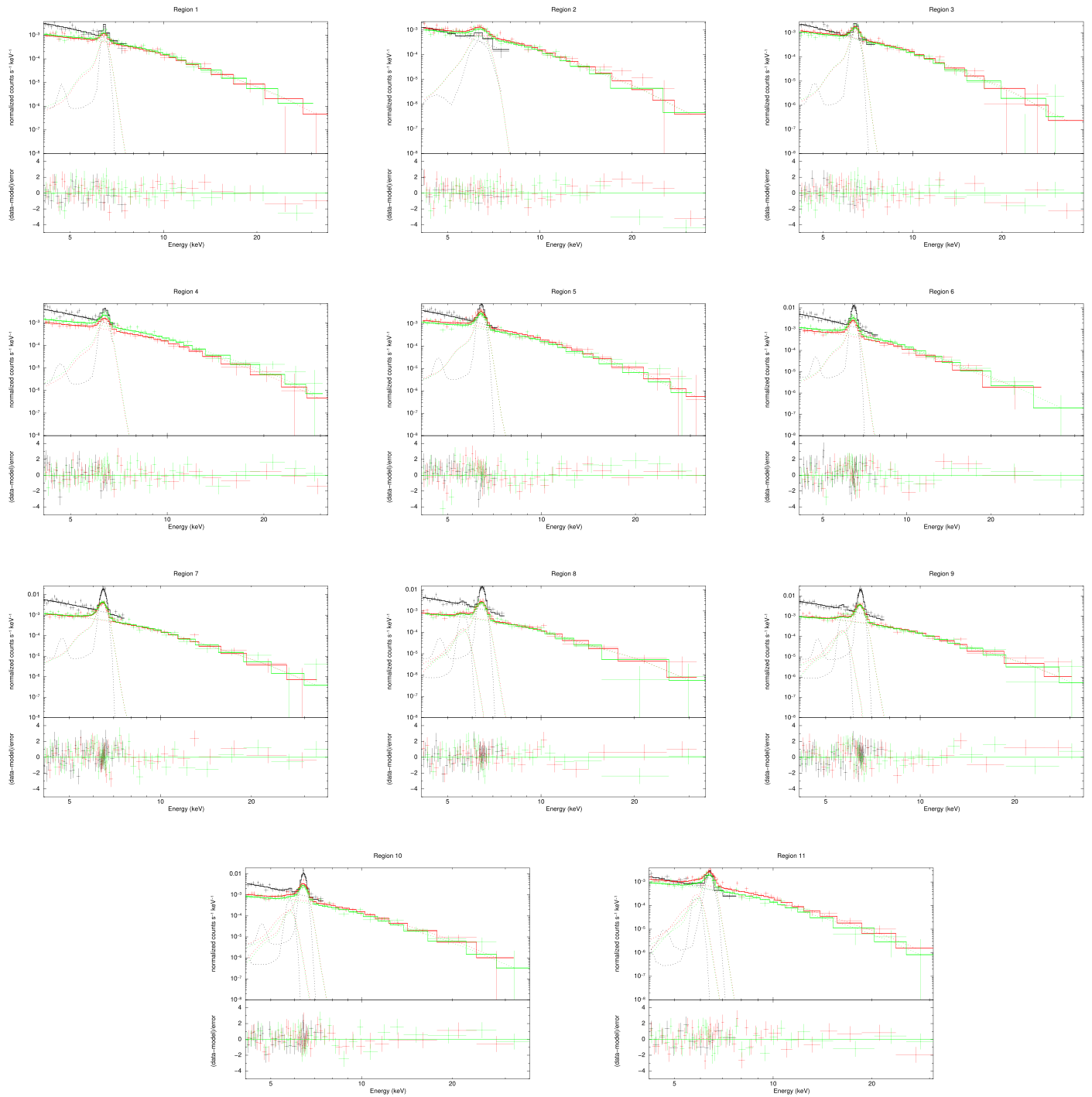

Figure 6. EPIC pn (black), FPMA (red), and FPMB (green) spectra extracted from regions 1–11 (see Figure 1) with the corresponding best-fit model and residual in the 4.1–30 keV band (see Table 2 for the best-fit values).
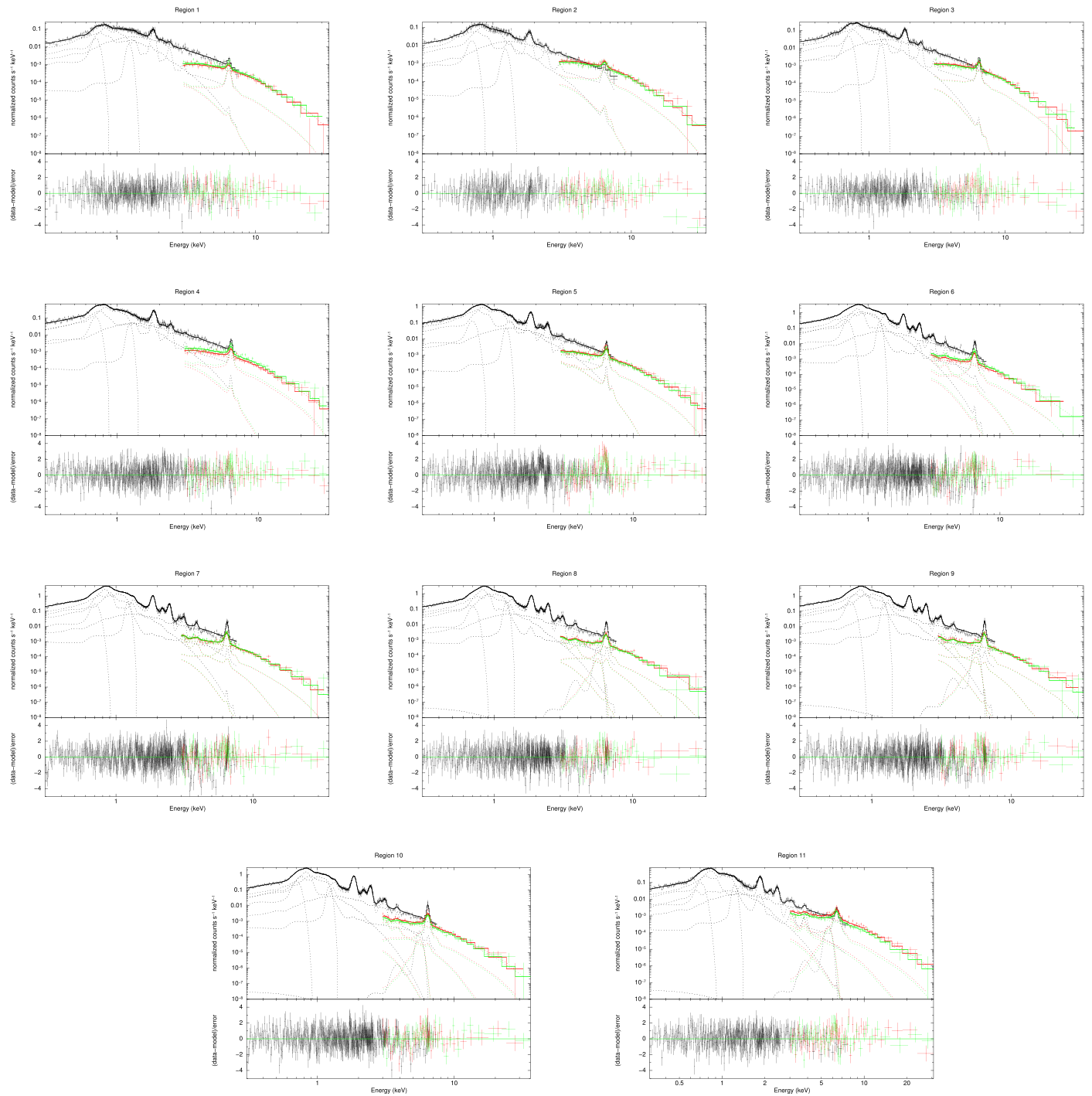
Figure 7. EPIC pn (black), FPMA (red), and FPMB (green) spectra extracted from regions 1–11 (see Figure 1) with the corresponding best-fit model and residual in the 0.3–30 keV band.

Appendix C
Proper Motion

To estimate the current velocity of the shock front in regions 1–11 (shown in Figure 1), we considered the proper-motion measurements by Coffin et al. (2022) and Katsuda et al. (2008). These measurements were obtained in small (with respect to our regions 1–11) regions at the shock front. For each region

we considered the closest region(s) by Coffin et al. (2022), when available, and by Katsuda et al. (2008) elsewhere, as shown in detail in Table 5. When more than one measurement of the proper motion was available, we considered their arithmetic mean. We did not find measurements of the proper motion in the areas of the shell corresponding to our regions 1 and 10.

Table 5
Match between Regions with Proper-motion Measurements Available in the Literature and Regions from This Work

Region #	Coffin et al. (2022) Region #	Katsuda et al. (2008) Region #
1	/	/
2	7	/
3	8–9	/
4	9	/
5	/	9-10-11
6	/	13
7	16	/
8	1	/
9	2	/
10	/	/
11	3–4	/

ORCID iDs

Vincenzo Sapienza ⓘ https://orcid.org/0000-0002-6045-136X
Marco Miceli ⓘ https://orcid.org/0000-0003-0876-8391
Aya Bamba ⓘ https://orcid.org/0000-0003-0890-4920
Satoru Katsuda ⓘ https://orcid.org/0000-0002-1104-7205
Yukikatsu Terada ⓘ https://orcid.org/0000-0002-2359-1857
Fabrizio Bocchino ⓘ https://orcid.org/0000-0002-2321-5616
Salvatore Orlando ⓘ https://orcid.org/0000-0003-2836-540X
Giovanni Peres ⓘ https://orcid.org/0000-0002-6033-8180

References

Acero, F., Lemoine-Goumard, M., & Ballet, J. 2022, A&A, 660, A129
Ackermann, M., Ajello, M., Allafort, A., et al. 2013, Sci, 339, 807
Aharonian, F., Akhperjanian, A. G., Barres de Almeida, U., et al. 2008, A&A, 488, 219
Aharonian, F. A., & Atoyan, A. M. 1999, A&A, 351, 330
Aleksić, J., Alvarez, E. A., Antonelli, L. A., et al. 2012, A&A, 541, A13
Anders, E., & Grevesse, N. 1989, GeCoA, 53, 197
Arnaud, K. A. 1996, in ASP Conf. Ser. 101, Astronomical Data Analysis Software and Systems, ed. G. H. Jacoby & J. Barnes (San Francisco, CA: ASP), 17
Axford, W. I., Leer, E., & Skadron, G. 1977, ICRC (Budapest), 11, 132
Bamba, A., Ueno, M., Nakajima, H., & Koyama, K. 2004, ApJ, 602, 257
Bamba, A., Yamazaki, R., Yoshida, T., Terasawa, T., & Koyama, K. 2005, ApJ, 621, 793
Bandiera, R. 1987, ApJ, 319, 885
Bell, A. R. 1978, MNRAS, 182, 147
Bell, A. R. 2004, MNRAS, 353, 550
Blair, W. P., Ghavamian, P., Long, K. S., et al. 2007, ApJ, 662, 998
Blandford, R. D., & Ostriker, J. P. 1978, ApJL, 221, L29
Cassam-Chenaï, G., Decourchelle, A., Ballet, J., et al. 2004, A&A, 414, 545
Chiotellis, A., Schure, K. M., & Vink, J. 2012, A&A, 537, A139
Coffin, S. C., Williams, B. J., & Katsuda, S. 2022, ApJ, 926, 84
DeLaney, T., Koralesky, B., Rudnick, L., & Dickel, J. R. 2002, ApJ, 580, 914
H. E. S. S. Collaboration, Abdalla, H., Abramowski, A., et al. 2018, A&A, 612, A5
Inoue, T., Yamazaki, R., Inutsuka, S. I, & Fukui, Y. 2012, ApJ, 744, 71
Kasuga, T., Vink, J., Katsuda, S., et al. 2021, ApJ, 915, 42
Katsuda, S., Tsunemi, H., Uchida, H., & Kimura, M. 2008, ApJ, 689, 225
Katsuda, S., Mori, K., Maeda, K., et al. 2015, ApJ, 808, 49
Kerzendorf, W. E., & Sim, S. A. 2014, MNRAS, 440, 387
Kinugasa, K., & Tsunemi, H. 1999, PASJ, 51, 239
Koyama, K., Petre, R., Gotthelf, E. V., et al. 1995, Natur, 378, 255
Lopez, L. A., Grefenstette, B. W., Auchettl, K., Madsen, K. K., & Castro, D. 2020, ApJ, 893, 144
Lopez, L. A., Grefenstette, B. W., Reynolds, S. P., et al. 2015, ApJ, 814, 132
Madsen, K. K., Beardmore, A. P., Forster, K., et al. 2017, AJ, 153, 2
Malkov, M. A., & Drury, L. O. 2001, RPPh, 64, 429
Miceli, M., Bocchino, F., Decourchelle, A., et al. 2013, A&A, 556, A80
Miceli, M., Decourchelle, A., Ballet, J., et al. 2006, A&A, 453, 567
Morlino, G., & Caprioli, D. 2012, A&A, 538, A81
Nagayoshi, T., Bamba, A., Katsuda, S., & Terada, Y. 2021, PASJ, 73, 302
Orlando, S., Bocchino, F., Reale, F., Peres, G., & Pagano, P. 2008, ApJ, 678, 274
Parizot, E., Marcowith, A., Ballet, J., & Gallant, Y. A. 2006, A&A, 453, 387
Prokhorov, D., Vink, J., Simoni, R., et al. 2022, ICRC (Berlin), 805
Rettig, R., & Pohl, M. 2012, A&A, 545, A47
Reynolds, S. P. 2008, ARA&A, 46, 89
Reynolds, S. P., Borkowski, K. J., Hwang, U., et al. 2007, ApJL, 668, L135
Reynolds, S. P., Williams, B. J., Borkowski, K. J., & Long, K. S. 2021, ApJ, 917, 55
Reynoso, E. M., & Goss, W. M. 1999, AJ, 118, 926
Ruiz-Lapuente, P., Damiani, F., Bedin, L., et al. 2018, ApJ, 862, 124
Sankrit, R., Raymond, J. C., Blair, W. P., et al. 2016, ApJ, 817, 36
Sano, H., Fukuda, T., Yoshiike, S., et al. 2015, ApJ, 799, 175
Sato, T., & Hughes, J. P. 2017, ApJ, 845, 167
Strong, A. W., Moskalenko, I. V., & Ptuskin, V. S. 2007, ARNPS, 57, 285
Tsuji, N., Uchiyama, Y., Khangulyan, D., & Aharonian, F. 2021, ApJ, 907, 117
Velázquez, P. F., Vigh, C. D., Reynoso, E. M., Gómez, D. O., & Schneiter, E. M. 2006, ApJ, 649, 779
Vink, J. 2008, ApJ, 689, 231
Vink, J. 2020, Physics and Evolution of Supernova Remnants (Cham: Springer)
Völk, H. J., Berezhko, E. G., & Ksenofontov, L. T. 2005, A&A, 433, 229
Xiang, Y., & Jiang, Z. 2021, ApJ, 908, 22
Yamaguchi, H., Bamba, A., & Koyama, K. 2009, PASJ, 61, S175
Yang, X. J., Tsunemi, H., Lu, F. J., et al. 2013, ApJ, 766, 44
Zabalza, V. 2015, ICRC (The Hague), 922
Zirakashvili, V. N., & Aharonian, F. 2007, A&A, 465, 695
Zirakashvili, V. N., & Aharonian, F. A. 2010, ApJ, 708, 965